AIAA JOURNAL
Vol. 45, No. 1, January 2007

Time-Series and Time-Averaged Characteristics of Subsonic to Supersonic Base Flows

Soshi Kawai*
University of Tokyo, Tokyo 113-8656, Japan
and
Kozo Fujii†
Japan Aerospace Exploration Agency, Kanagawa 229-8510, Japan

DOI: 10.2514/1.24601

Physics of cylindrical base flows ranging from subsonic to supersonic speeds at zero angle of attack are computationally investigated. Time-series and time-averaged investigations of base flows show distinctive characteristics at subsonic, transonic, and supersonic regimes. Normalized time-averaged base pressure decreases proportionally with respect to increasing freestream dynamic pressure in the subsonic regime of $M_\infty < 0.8$. The base pressure begins to fall rapidly in the transonic regime and then settles down and decreases gradually toward an asymptotic value at $M_\infty > 1.5$. Normalized base pressure fluctuations sharply increase at transonic speeds, whereas they decrease with increasing freestream Mach number at subsonic and supersonic speeds. Appearance of unsteady local shock waves change the characteristics of base pressure distinctively at the transonic speeds. Spectra of the base pressure show one clear peak at subsonic speeds (related to the shear layer dynamics), two clear peaks at transonic speeds (related to the shear layer dynamics and its subharmonic), and three major peaks at supersonic speeds (related to the shear layer dynamics, its subharmonic, and an additional mechanism). Instability of the free shear layers has dominant influence on the overall base flowfield over a wide range of Mach numbers ranging from subsonic to supersonic speeds. However, at supersonic speeds, an additional mechanism of instability within the recirculating region is possibly at work and has dominant influence on the flowfield. The dominant mechanisms significantly cause the strong Mach number dependence of the high-pressure region which is strongly related to the base pressure. The spectrum analysis suggests that the substantial base pressure fluctuations are caused by the pulsing of the flow inside the recirculating region.

Nomenclature

a	=	sonic speed
C_K	=	Yoshizawa model coefficient
C_p	=	local pressure coefficient
C_S	=	Smagorinsky model coefficient
C_x	=	axial force coefficient
D	=	cylinder base diameter
d_{blend}	=	distance from closest wall to blending position
d_{wall}	=	distance from closest wall
M	=	local Mach number
Pr_t	=	turbulent Prandtl number
p	=	local static pressure
q	=	local dynamic pressure
$\boldsymbol{q_j}$	=	heat flux vector
R	=	cylinder base radius
Re	=	Reynolds number
S_{ij}	=	strain rate tensor
Sr	=	Strouhal number
T	=	temperature
u	=	axial velocity
x, y, z	=	Cartesian coordinates
$\boldsymbol{x_j}$	=	coordinate vector
γ	=	ratio of specific heats
Δ_{filter}	=	filter length scale
Δt	=	integration time
$\Delta x, \Delta y, \Delta z$	=	step size of the grid in x, y, z directions
δ_{ij}	=	Kronecker delta
μ_t	=	turbulent eddy viscosity
ν	=	kinematic eddy viscosity
ρ	=	density
$\Gamma(\eta)$	=	blending function

Superscripts

LES	=	quantity in large-eddy simulation formulation
RANS	=	quantity in Reynolds-averaged Navier–Stokes formulation
$*$	=	dimensional quantity
$\bar{}$	=	spatial-filtered or ensemble-averaged quantity
$\tilde{}$	=	Favre-filtered or Favre-averaged quantity
$+$	=	wall unit quantity

Subscripts

∞	=	freestream quantity

Received 13 April 2006; revision received 26 August 2006; accepted for publication 4 September 2006.

*Research Fellow of Japan Society for the Promotion of Science, Department of Aeronautics and Astronautics, 3-1-1 Yoshinodai, Sagamihara, Kanagawa 229-8510, Japan; Corresponding Author, E-mail: kawai@fla-b.eng.isas.jaxa.jp. Member AIAA.

†Professor, Institute of Space and Astronautical Science, Department of Space Transportation Engineering, 3-1-1 Yoshinodai, Sagamihara, Kanagawa 229-8510, Japan. Fellow AIAA.

I. Introduction

BASE flows are geometrically simple and at first glance are often considered to be simple constructions of free shear layer, recirculating region, etc. Boundary layers that develop along the lateral surface of the body separate at the base edge, and the turbulent free shear layer appears. A recirculating region is generated downstream of the base where the pressure becomes relatively low compared with that of the freestream, as shown in Fig. 1. Mach

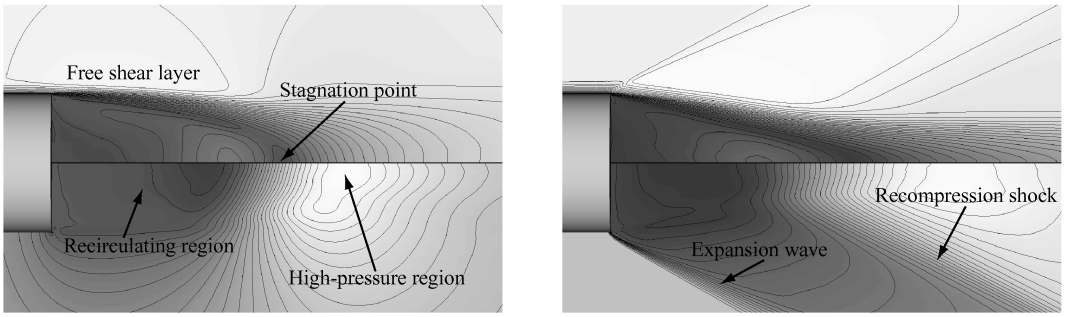

a) Subsonic flow region **b) Supersonic flow region**

Fig. 1 Schematic of time-averaged axisymmetric base flows.

number distributions are shown in the upper half of the figure and static pressure distributions are shown in the lower half. When the freestream Mach number increases from subsonic to supersonic, the flow expands at the base edge and a recompression shock wave is generated downstream.

The base pressure of a projectile, rocket, reentry capsule, aerospike nozzle, reusable launch vehicle, etc., (powered or not) is usually noticeably lower than the freestream pressure and can cause significant base drag and degrade the aerodynamic performance of the vehicle. Moreover, fluctuations of the base pressure can sometimes cause dynamic instability of such vehicles. Rollstin [1] showed in his in-flight base pressure measurements for a 155 mm projectile configuration that up to 35% of the total drag is contributed by the base drag at supersonic speeds. Computations for a typical shell at Mach number from 0.9 to 1.2 also indicate that the base drag accounts for up to 50% of the total drag [2]. Numerical investigations of the dynamic instability of a blunt and short reentry capsule at transonic speeds show that the instability of the capsule is primarily caused by the phase delay of the base pressure [3]. Such results clearly indicate the importance of understanding base flowfields over a wide range of Mach numbers. The complete understanding of base flow phenomena, especially their dependence on the Mach number, yields useful information for the design of a vehicle. The knowledge of base flows may lead to the ability to control the near-wake flow interactions as well as to control and minimize the base drag, and thus enhance the overall vehicle stability.

Because of the importance of understanding the base flows, various experimental and numerical approaches have been performed in the past. Traditional wind-tunnel tests usually used a support sting from the rear of a test model. No matter how small its diameter, the presence of the support sting largely destroys the flow structure behind the test model near its wake axis. The strong interactions occurring at the wake neck contain primary physical mechanisms that determine the base pressure. Therefore, traditional wind-tunnel tests are not adequate for investigating base flowfields and base drags. As a result, in-flight tests have been mostly adopted in the past as a reliable experimental method. During in-flight tests, a spark shadowgraph of a nine-degree half-angle cone with sharp nose at a freestream Mach number of 4.81 revealed many detailed features of the flow in the shock layer, the boundary layer, and the base region [4]. Mach number dependence of base pressure were experimentally investigated by Merz et al. [5] at subsonic speeds, Chow [6] at transonic speeds, and Bulmer [7] and Zarin [8] at supersonic and hypersonic speeds. These experimental investigations demonstrated that the base pressure coefficient is relatively constant at freestream Mach numbers between 0.0 and 0.8, but begins to fall rapidly as the flow approaches sonic speed. The base pressure, normalized by its freestream value, gradually decreases with increasing freestream Mach number at supersonic speeds. Even with these experimental results, however, it is not clear how the base flow phenomena affect the base pressure over a wide range of Mach numbers.

To reduce the base drag and enhance the vehicle aerodynamic performance, a more complete understanding of base flows is desired. Recently, extensive experimental investigations of a supersonic base flow at a freestream Mach number of 2.46 have been successfully performed by the University of Illinois Gas Dynamics Laboratory [9–12] with their supersonic wind tunnel designed specifically for the study of cylindrical base flows. The experiments included time-averaged base surface pressure measurements, mean velocity and Reynolds stress, detailed flow laser Doppler velocimetry, particle image velocimetry measurements downstream of the base, planar Mie/Rayleigh scattering visualizations of the shear layer and developing wake, and time-series of base pressure measurements. Supersonic base flow features at $M_\infty = 2.46$ have been revealed in detail from the various types of measurements. However, these investigations are still limited to the supersonic speed of $M_\infty = 2.46$. Detailed base flow phenomena associated with the base pressure over a wide range of Mach numbers have not yet been investigated. Such experimental investigations are restricted by the requirement of a specifically designed wind tunnel and difficulties in obtaining various types of flow data. Concerning these difficulties in the experiments, a numerical approach is an attractive choice because it eliminates any subject interference with the flowfields and supplies a wide range of flow data, whereas only limited data can be easily obtained by the experiments.

As for an analysis using computational fluid dynamics, difficulties still remain in the simulation of turbulence which appears in most flows encountered in engineering practice. Simulation of base flows, where a turbulent boundary layer develops along the lateral surface of a body and turbulent mixing occurs downstream of the base, represents such a case. There have been various CFD studies for the prediction of base flows and most of them used Reynolds-averaged Navier–Stokes (RANS) simulations with RANS turbulence models to handle high Reynolds number flows. Many investigations with various RANS turbulence models have tried to predict the supersonic cylindrical base flow [13–16], an axisymmetric truncated plug nozzle [17,18], and blunted cone cylinder [19]. Some improvements of the predictability have been made, but unfortunately the RANS simulations have failed to produce quantitative prediction of the base flow. Base flows include large and small eddy structures in the wake, which produces strong unsteadiness in the flow. This is considered to be the main reason that RANS simulations with RANS turbulence models do not give satisfactory results. Thanks to the rapid progress in the capability of computers, large-eddy simulation (LES) is regarded as a promising alternative. As for the prediction of the supersonic base flow, prediction accuracy has been improved by the unsteady computations using LES [20] and monotone integrated large-eddy simulation (MILES) [21]. These results have shown that LES and MILES approaches seem to be effective for the base flow analysis compared with conventional RANS. However, both LES and MILES require extremely fine mesh resolution with an enormous amount of grid points near wall regions for the simulation of high Reynolds number flows. In addition, to maintain temporal accuracy inside the boundary layers, computational time-step size is limited by the extremely fine mesh near walls. Under the restriction of present or near-future computer environment, LES and MILES are not or will not be an easy approach for the analysis of base flows at realistic Reynolds numbers.

To overcome the disadvantages of RANS and LES and to investigate base flows over a wide range of Mach numbers, we have

been working on the development of multiple simulation codes named LES/RANS hybrid methodology which combines the advantages of LES and RANS into one model. The LES/RANS hybrid approach applies a RANS computation based on ensemble-averaged Navier–Stokes equations to the regions near solid surfaces, whereas an LES computation based on spatially-filtered Navier–Stokes equations is applicable to other regions that may include massively separated flows. There is a similar approach named detached-eddy simulation [22] (DES) that resembles such method. However, DES does not combine LES and RANS computations in the system as the present LES/RANS hybrid method does; instead, it is simply a modification of the Spalart–Allmaras turbulence model [23]. For the hybrid code, because small-scale turbulence at wall-bounded regions is fully modeled in RANS simulation, grids are not necessary to cluster near the wall in streamwise and spanwise directions as required in LES. Therefore, the advantages of the LES/RANS hybrid methodology are that it can alleviate immense grid requirements and severe time-step limitation associated with the small-eddy motions which need to be resolved in near-wall regions in LES. As a result, the hybrid method requires much less computational cost than that of the LES approach. The authors have already developed and applied the LES/RANS hybrid methodology to the supersonic base flows of Herrin and Dutton and subsonic flows around a thin-airfoil near stall [24,25]. The results successfully demonstrated that the LES/RANS hybrid methodology is more practical and efficient than that of a pure LES approach in predicting high Reynolds number compressible and turbulent flows.

In the present study, time-series and time-averaged characteristics of cylindrical base flows from subsonic to supersonic speeds at zero angle of attack are computationally investigated with the LES/RANS hybrid methodology. The primary purpose of this paper is to understand base flow mechanisms associated with the base pressure over a wide range of Mach numbers. The reliability of the present hybrid method for a supersonic base flow has been confirmed in our previous study [24]; reliability for the case of subsonic base flows is investigated by comparing with the experiments of Merz et al. [5].

II. Problem Settings

To clearly understand the essential mechanisms of base flows, a cylindrical object set at 0 deg angle of attack was chosen for the present study. In this simple configuration, a separation line is fixed at the base edge and an approaching boundary layer develops smoothly along the lateral surface of the body.

We focus on the Mach number range from subsonic to supersonic speeds because at such speed range, the aerodynamic characteristics of vehicles depend highly on the low-pressure distributions on the base. Base flows in hypersonic speeds are not discussed in this paper because aerodynamic characteristics at hypersonic speeds can be well estimated by the Newtonian method. In our study, the flowfield is considered to be fully turbulent, and high Reynolds numbers (based on the base diameter) in the order of 10^6 are chosen.

III. Mathematical Models

A. LES/RANS Hybrid Methodology

Both Favre-filtered and Favre-averaged Navier–Stokes equations, which are the governing equations for LES and RANS, respectively, are derived from the compressible form of Navier–Stokes equations for the development of LES/RANS hybrid methodology. The details of these derivations are provided in [26,27]. Both Favre-filtered and -averaged Navier–Stokes equations for an ideal gas are non-dimensionalized by the density, the speed of sound of the freestream, and the characteristic length D, and then transformed to the generalized curvilinear coordinate system. In the present LES/RANS hybrid methodology, the governing equations of RANS are applied to regions near solid surfaces inside the boundary layers, whereas the governing equations of LES are applied to the massively separated flow regions. Motivation of the present hybrid method is to alleviate the immense grid requirements and the resulting severe time-step limitation in the wall-bounded regions. Sutherland's law is used to compute molecular dynamic viscosity. Prandtl number and specific heat ratio are fixed at 0.72 and 1.4, respectively.

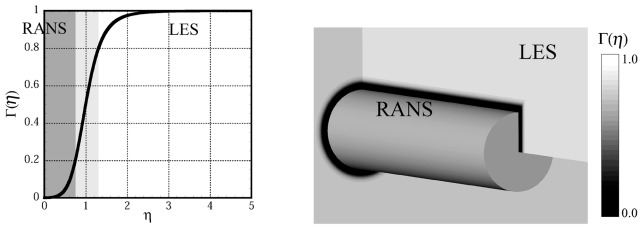

a) Behavior of blending function with η **b) Distribution of blending function around the base**

Fig. 2 Blending of LES and RANS formulation sets with buffer region.

Near the interface of LES and RANS regions, LES formulation and RANS formulation sets are blended with a buffer region by the following method:

$$[\text{LES/RANS hybrid}] = \Gamma(\eta)[\text{LES}] + [1 - \Gamma(\eta)][\text{RANS}] \qquad (1)$$

The blending function used in the present study is defined as

$$\Gamma(\eta) = \frac{1}{2} + \tanh\left(\frac{C_1(0.2\eta - C_2)}{0.2(1 - 2C_2)\eta + C_2}\right)/2\tanh(C_1) \qquad (2)$$

where the function changes from 0 to 1 as shown in Fig. 2a. In Eq. (2), $\eta = d_{\text{wall}}/d_{\text{blend}}$, $C_1 = 4$, and $C_2 = 0.2$. A similar expression is used for the weighting function of inner and outer regions in the boundary layers [28]. The parameter C_1 controls the blending width of the LES and RANS regions where the function changes from 0 to 1 as shown in Fig. 2. For the blending function $\Gamma(\eta) = 0.5$ at $\eta = 1.0$, C_2 is set to be 0.2 in this study. Under the condition of $C_1 = 4$ and $C_2 = 0.2$, transition from RANS near the solid surface to LES is smoothly designed around the location specified from the surface of the wall with Eq. (2) and the value rapidly increases to 1.0 away from the boundary layer edge. It is not appropriate to set the d_{blend} less than the thickness of the boundary layer and to set a blending position within the boundary layer because the LES region appears near the solid surface and immense grid points are required to resolve the near-wall turbulence. Increasing the required grid points inside the boundary layer would lose the advantage of the present hybrid method. Therefore, d_{blend} is fixed to be approximately the maximum boundary layer thickness. The effects of the RANS should be rapidly diminished outside of the boundary layer edge as the present choice of the constant of $C_1 = 4$ realizes, because the predictability of the RANS in the massively separated flow region is not as good as the one in the turbulent boundary layer. In this study, d_{blend} is specified from a priori RANS simulation. Distribution of the value of the blending function around the base is shown in Fig. 2b.

Time-averaged quantities in the RANS formulation are fundamentally different from spatially-filtered quantities in the LES formulation. Therefore, theoretical contrariety does exist in the present hybrid methodology. However, because of the similar form of the governing equations in the RANS and LES formulations, both formulation sets can be solved continuously with a single computational method. The present LES/RANS hybrid approach is different from the zonal approach in the sense that single grid and formulation is used in the simulation. We are expecting the RANS-to-LES region to change from fully modeled stresses given by a RANS turbulence model to resolved stresses which appear when an unsteady flow is averaged, as discussed in [29].

The present LES/RANS hybrid methodology employs a RANS approach to provide ensemble-averaged flow characteristics of the wall boundary layers (black region in Fig. 2b). The flow downstream of the base-edge separation is then simulated using LES (white region in Fig. 2b). Although the upstream RANS approach does not provide any unsteady turbulent information to the mixing layer downstream, the effects of ensemble-averaged flow quantities are provided to the LES region. Theoretical contrariety and the lack of turbulent fluctuations in the RANS region are limits of the LES/

RANS hybrid methodology. However, successful predictions of qualitative instantaneous flowfield and detailed time-averaged flow quantities behind the base were achieved in spite of the limitations, as shown in [24].

B. Turbulence Modeling

1. LES Turbulence Modeling

The subgrid-scale (SGS) turbulent stress tensor used in the present study is based on the Smagorinsky model [30] because of its robustness and low computational cost. The Smagorinsky eddy viscosity formulation for the turbulent stress tensor ϕ_{ij} is

$$\bar{\rho}\phi_{ij} - \frac{1}{3}\delta_{ij}\bar{\rho}\phi_{ii} = -2\mu_t^{\mathrm{LES}}\tilde{S}_{ij} = -2\bar{\rho}C_S^2\Delta_{\mathrm{filter}}^2|\tilde{S}|\tilde{S}_{ij} \tag{3}$$

The SGS eddy viscosity μ_t^{LES} is analogous to the eddy viscosity used in a RANS turbulence model and is written as

$$\mu_t^{\mathrm{LES}} = \bar{\rho}C_S^2\Delta_{\mathrm{filter}}^2|\tilde{S}| \tag{4}$$

Δ_{filter} in Eq. (3) is chosen to be the characteristic length of the computational grid. This length varies over a grid because of its nonuniform nature. To properly account for the grid anisotropy, Deardorff's determination of Δ_{filter} with modification by the anisotropy correction of Scotti and Meneveau [31] is introduced in the present study. The filter length scaled at each grid point is evaluated by the following formulas:

$$\Delta_{\mathrm{filter}} = (\Delta x\Delta y\Delta z)^{-1/3} f(a_1, a_2) \tag{5}$$

$$f(a_1, a_2) = \cosh\sqrt{\frac{4}{27}[(\ell_n a_1)^2 - \ell_n a_1\,\ell_n a_2 + (\ell_n a_2)^2]} \tag{6}$$

where $f(a_1, a_2)$ is the function of the grid aspect ratios a_1 and a_2; a_1 and a_2 are defined by the two smallest aspect ratios, $a_1 = \Delta_i/\Delta_{\max}$, $a_2 = \Delta_j/\Delta_{\max}$, $\Delta_{\max} = \max(\Delta_x, \Delta_y, \Delta_z)$.

Additional terms necessary for determining compressibility are modeled based on the work of Yoshizawa [32], Moin et al. [33], Vreman [26], and Vreman et al. [34–36]. The Yoshizawa model [32] is applied to the computation of an isotropic part of the SGS stress tensor

$$\bar{\rho}\phi_{ii} = 2\bar{\rho}C_K\bar{\Delta}_{\mathrm{filter}}^2|\tilde{S}|^2 \tag{7}$$

The eddy diffusivity model is applied to the SGS heat flux term

$$\boldsymbol{q}_j^{\mathrm{LES}} = -\frac{\partial}{\partial \boldsymbol{x}_j}\left(\frac{\mu_t^{\mathrm{LES}}}{(\gamma-1)Pr_t^{\mathrm{LES}}M^2}\frac{\partial\tilde{T}}{\partial \boldsymbol{x}_j}\right) \tag{8}$$

where the SGS turbulent Prandtl number Pr_t^{LES} is fixed to 0.9. In the present study, other SGS terms are neglected based on the work of Moin et al. [33] and Vreman [26].

It is necessary to set the values of the Smagorinsky and Yoshizawa constants in advance because they are not universal constants in the LES simulations of various types of turbulent flows. Therefore, the constants for the SGS model are chosen based on previous studies. Vreman et al. [36] derived a relation between C_S and C_K, $C_K \geq \sqrt{3}C_S^2/2$. The inequality of Vreman et al. suggests a necessary condition for realizability of the SGS stress tensor. Yoshizawa [32] proposed $C_S = 0.16$ and $C_K = 0.0886$ from two-scale-direct-interaction-approximation. Rogallo and Moin [37] suggested the range of the Smagorinsky constant $0.10 \leq C_S \leq 0.24$. The consideration about the Smagorinsky constant for a compressible turbulent flow analysis in our previous study of supersonic base flows demonstrated that the adequate value of the Smagorinsky constant may be larger in flows with strong compressibility than in incompressible flows, and the resultant value of the Smagorinsky constant of $C_S = 0.24$ showed successful agreements with the experiment [24]. Based on the previous studies, $C_S = 0.24$ and $C_K = 0.0886$ are chosen for the present study. These constants clearly satisfy the inequality equation of Vreman et al. [36] and the range of $0.10 \leq C_S \leq 0.24$.

2. RANS Turbulence Modeling

The Boussinesq approximation is used to relate the turbulent Reynolds stress $\overline{\rho u_i' u_j'}$ to the rate of strain tensor through a RANS turbulent eddy viscosity

$$-\overline{\rho u_i' u_j'} = \mu_t^{\mathrm{RANS}}\tilde{S}_{ij} \tag{9}$$

where the RANS eddy viscosity μ_t^{RANS} is analogous to the eddy viscosity μ_t^{LES} used in LES. The turbulent eddy-viscosity coefficient μ_t^{RANS} is evaluated from a RANS turbulence model. The RANS turbulence model used in the present study for compressible flow analyses is based on the Baldwin–Lomax algebraic eddy-viscosity model [38] because of its robustness and low computational cost. These characteristics in the LES and RANS turbulence models often become prominent advantages when the LES/RANS hybrid method is applied to practical problems.

Similar to the LES modeling, the RANS turbulent heat flux is related to the temperature gradient through a turbulent conductivity and is also expressed as a function of the turbulent viscosity μ_t^{RANS},

$$\boldsymbol{q}_j^{\mathrm{RANS}} = -\frac{\partial}{\partial \boldsymbol{x}_j}\left(\frac{\mu_t^{\mathrm{RANS}}}{(\gamma-1)Pr_t^{\mathrm{RANS}}M^2}\frac{\partial\tilde{T}}{\partial \boldsymbol{x}_j}\right) \tag{10}$$

The RANS turbulent Prandtl number Pr_t^{RANS} is taken as constant here and is equal to 0.9.

C. Numerical Scheme

Based on our previous study [24], the equations are solved in generalized curvilinear coordinates and the numerical fluxes are evaluated by the high-resolution upwind scheme [39] which belongs to the family of advection upstream splitting-method-type schemes to avoid numerical instability at the flow discontinuity. Physical properties at the grid interface are evaluated by the monotone upwind scheme for conservation law interpolation [40] based on primitive variables to achieve third-order space accuracy on an evenly spaced grid. The viscous terms are evaluated by a second-order central differencing scheme. Our previous study [24] showed that the present LES/RANS hybrid methodology, coupled with the present numerical scheme, successfully provided the essential features of base flows which we focus on in the present study from an engineering viewpoint.

The flowfield considered here is unsteady, and therefore it is necessary to resolve the unsteady flow in both time and space in the present LES/RANS hybrid methodology. The local Courant–Friedrichs–Lewy (CFL) number must be kept at a magnitude of order of unity [41] or an appropriate number of inner iterations must be used for the implicit time integration method. In addition to the temporal accuracy, the total simulation time (time-step size× total iteration number) is also important because flow quantities need to be computed by simulating and averaging the unsteady flowfield for a sufficiently long time. A lower-upper symmetric Gauss–Seidel (LU-SGS) factorization implicit algorithm [42] is used for the time integration in this study to overcome the restriction of the time-step size. Although the LU-SGS implicit time integration scheme is numerically efficient, the temporal accuracy of the scheme is less than the first-order due to the errors of linearization. To minimize such errors, a three-level backward-differencing formula is employed for achieving second-order temporal accuracy and multiple subiterations (Newton–Raphson iteration) [43] are adopted. In the present study, the global computational time-step $\Delta t = \Delta t^* \cdot a_\infty^*/D^*$ is set to be less than 0.005 in all cases and three subiterations are sufficient to achieve a two-order reduction of the residual. In all cases, the local CFL number at the interface of the RANS and LES regions is less than 0.45 for the chosen time-step. The local CFL number in the LES region is sufficiently less than unity.

Table 1 Computational flow conditions

	Subsonic speeds based on Merz et al. [5]				Supersonic speeds					
M_∞	0.52	0.66	0.80	0.94	1.05	1.20	1.50	2.00	3.00	4.00
Re ($\times 10^5$)	4.3	5.1	5.7	6.1	10.0					

D. Boundary Conditions

A compressible flow extension of the rescaling–reintroducing method introduced by Urbin and Knight [44] is used for inflow boundaries. In this method, the flowfield at a downstream station, $3D$ downstream from the inflow boundary, is rescaled and reintroduced at the inflow condition. The thickness of the approaching boundary layer greatly influences the base flowfield as shown in our previous study [24], as it determines the gradient of the initial shear layer and, therefore, the growth rates of the shear layer instabilities. The inflow boundary layer thickness at $4D$ upstream from the base plane is fixed at $0.138R$ for all cases in the present study, and there is little difference in the thickness of the approaching boundary layer just before the base edge separation. For the chosen thickness of the inflow boundary layer, simulated boundary layer velocity profile at $2D$ downstream from the inflow boundary well represents the available experimental data [5] as shown in [45]. For subsonic outflow and external boundaries, the pressure is fixed at the freestream value and other physical variables are specified by the zero-gradient condition. For supersonic outflow and external boundaries, all physical variables are specified by the zero-gradient condition. Solid wall boundary condition at the cylinder surface is treated as no-slip. In addition, density is extrapolated from an adjacent node, and pressure is defined from the equilibrium condition of the momentum normal to the wall. Properties along a single line at the wake axis are averaged from the variables at the nodes around the axis. Periodic boundary condition is adopted in the azimuthal direction.

IV. Computational Setup

A. Flow Conditions

The computational flow conditions are summarized in Table 1. The flow conditions at the subsonic speeds are based on the experiments of subsonic cylindrical base flows of Merz et al. [5]. At supersonic speeds, the Reynolds number based on the cylinder diameter is fixed at 1.0×10^6 for each freestream Mach number. A total of ten computational cases were investigated, four cases at subsonic speeds and six at supersonic.

B. Computational Grid

The grid designed for the present study is topologically of O–O type as shown in Fig. 3. The computational domain extends $4D$ upstream and $20D$ downstream from the base plane and $20D$ radially from the cylinder lateral surface to the outer boundary. The axisymmetric grid consists of 149 points along the cylinder solid surface, 105 points in the azimuthal direction, and 189 points in the direction normal to wall. In the focused region behind the base, 92 points along the base surface and 166 points in the direction normal to wall are concentrated and the stretching of the grid is designed to be fairly small. Total number of grid points is approximately 2.96 million. A grid sensitivity study and resolved energy spectrum in our previous study [24] for the base flow of $M_\infty = 2.46$ and $Re = 2.858 \times 10^6$ showed that the present mesh resolution with the present spatial discretization scheme is adequate to simulate the essential feature of base flows. As for the cases of lower Mach number, the present mesh resolution is also expected to be adequate because the chosen Reynolds numbers are smaller than that in our previous study.

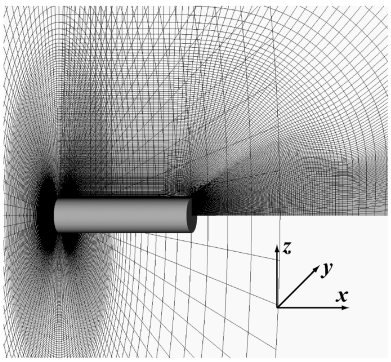

Fig. 3 Computational grid.

C. Data Processing

The flow configuration considered in this study, such as the shape of the object or the flow conditions, is relatively simple. However, the resultant flow field is rather complicated and shows unique characteristics. Therefore, time-series and time-averaged characteristics of the base pressure and the base flowfield are investigated to help clearly determine the flow mechanisms that dominate the time-series and time-averaged base pressure.

1. Time-Series Data Processing

Time-series flow data consist of data from approximately 400,000 time-steps. These data are extracted in each computational time-step and are reduced by a discrete Fourier transform (DFT) algorithm. Before the execution of the DFT, time-series data are modified by two data-grooming operations to improve the results of the power-spectral-density (PSD) estimations. These data sets are multiplied by a Hanning window to suppress side-lobe leakage of the DFT. The data segments are overlapped by 50% to reduce the increased normalized random error caused by the Hanning window as adopted in the experimental PSD estimations of base pressure fluctuations [12]. The DFT computations are performed at every radial grid point at a specific position for each data segment, and the final PSD is averaged over the radial locations and data segments. The frequency resolution of thePSD is approximately $\Delta Sr = 0.0015$ in all computational cases of the present study.

2. Time-Averaged Data Processing

The present computational time-step corresponds to approximately $\Delta t^* = 2.89 \times 10^{-7}$ s in dimensional time; it is based on the base diameter and the freestream speed of sound in the experiments [5]. Time-averaged data are computed by averaging the flowfields over about 120,000 steps (600.0 in normalized computational time, $t = t^* \cdot a^*_\infty / D^*$, and 34.7 ms in physical time) of unsteady flow simulations. Time-averaged data discussed in the following sections are averaged in time and over all azimuthal locations.

V. Numerical Results

Discussions of the Mach number dependence of the base pressure and the location and magnitude of the highest pressure in the developing wake are given first. These investigations characterize the base pressure as a function of freestream Mach number and high-pressure regions. Time-series characteristics of the base pressure and time-series and time-averaged characteristics of base flowfields at subsonic, transonic, and supersonic speeds are then discussed. These results would clearly determine the base flow mechanisms which contribute to the Mach number dependence of the base pressure.

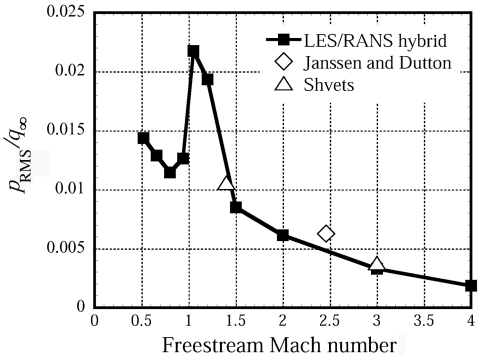

Fig. 4 Mach number dependence of RMS base pressure fluctuation levels on base surface.

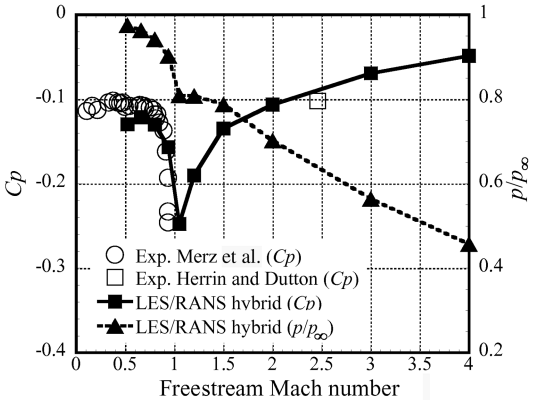

Fig. 5 Mach number dependence of time-averaged base pressure.

A. Mach Number Dependence of Base Pressure

One of the most important issues of base flows is the drag force produced by low base pressure that is a function of the freestream Mach number. Mach number dependence of root-mean-square (rms) base pressure fluctuations at $R/2$ radially on the base surface is shown in Fig. 4, where the symbols represent the experimental data of Janssen and Dutton [12] and Shvets [46]. In this figure, the rms base pressure fluctuations are normalized with respect to the freestream dynamic pressure. In Fig. 5, the time-averaged base pressure coefficient is plotted on the left axis and the normalized base pressure is plotted on the right axis; the experimental data over an entire subsonic range of Merz et al.[5] and the supersonic speed of Herrin and Dutton [9] are also plotted. The computational results agree reasonably well with the past experiments in the characteristics of fluctuation and time-averaged base pressure. These results validate the present LES/RANS hybrid methodology and furthermore add on its reliability that was first established in our previous study for the case of a supersonic base flow [24]. The agreements between the rms base pressure fluctuation levels and the instantaneous turbulent structures obtained in our past study [24] mean that the LES/RANS hybrid simulation is capable of representing the essential aspect of the unsteady base flow phenomena.

As clearly shown in Figs. 4 and 5, rms base pressure fluctuation and time-averaged base pressure display distinctive characteristics when the freestream Mach number increases from subsonic to supersonic. The base pressure fluctuations rise rapidly when the flow approaches sonic speed but decrease with increasing freestream Mach numbers below 0.8 and beyond 1.5. The normalized time-averaged base pressure decreases almost proportionally with respect to the increasing dynamic pressure ($C_p = \text{constant}$) at subsonic speeds. It rapidly falls as the flow approaches sonic speed, and then maintains almost the same value at transonic regime. As the flow reaches supersonic, the normalized base pressure gradually decreases toward an asymptotic value.

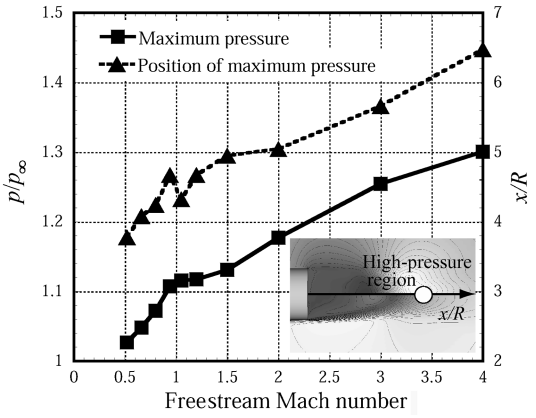

Fig. 6 Mach number dependence of time-averaged high-pressure region.

B. Mach Number Dependence of High-Pressure Region

The Mach number dependence of a time-averaged high-pressure region downstream of the base is shown in Fig. 6. In the figure, the maximum time-averaged pressure in the developing wake is normalized by the freestream pressure and plotted on the left axis, and its location downstream of the base surface is plotted on the right axis. Similar to the Mach number dependence of base pressure, the high-pressure region also shows distinctive characteristics when the flow speed increases from subsonic to supersonic. The magnitude of the highest pressure increases with increasing freestream Mach number at subsonic and supersonic speeds, but maintains almost the same value at transonic speeds. The location of the high-pressure region rapidly moves toward the base when the flow approaches sonic speed. In contrast, such location gradually moves downstream with increasing freestream Mach number at subsonic and supersonic speeds.

The characteristics of the base pressure are usually influenced by many factors in the complex flow, such as the condition of an approaching turbulent boundary layer, the process of turbulent mixing in the free shear layer, and compressibility of the flow. However, our previous simplified finding [24] showed that time-averaged base pressure is strongly related to the pressure level and the location of the high-pressure region. The high-pressure region is deemed to be the key factor in determining the strength of the circulating flow and the size of the recirculating region. As for the contribution of the high-pressure region, from a time-averaged viewpoint, when the pressure level at the high-pressure region is fixed and its location is closer to the base, a smaller recirculating region with stronger circulating flow is induced. In addition, when the pressure level increases but its location stays fixed, stronger circulating flow can also be induced. In both cases, the strong circulating flow results in the decrease of the base pressure and thus increases the base drag. The presence of a base cavity has proven to be effective in reducing the base drag in several previous experimental studies [47,48]. Such reduction of base drag can be easily explained by the lengthened downstream position of the high-pressure region in the presence of the base cavity. Such phenomenon induces a relatively large recirculating region accompanied with weak circulating flow near the base. As a result, the base pressure increases and the base drag decreases.

Mechanism of the strong Mach number dependence of the base pressure as shown in Figs. 4 and 5 can also be simply explained by the Mach number dependence of the high-pressure region along the wake axis, as shown in Fig. 6. Overall, the high-pressure region tends to shift downstream with increasing freestream Mach number. In such case, a relatively large recirculating region with weak flow is expected. However, in spite of the effect of the location, the increasing pressure level at the high-pressure region effectively induces strong circulating flow. The gradual base pressure decrease with increasing Mach number at subsonic and supersonic speeds is caused by this phenomenon. The rapid decrease in base pressure and the sharp increase in rms base pressure fluctuation at transonic speeds

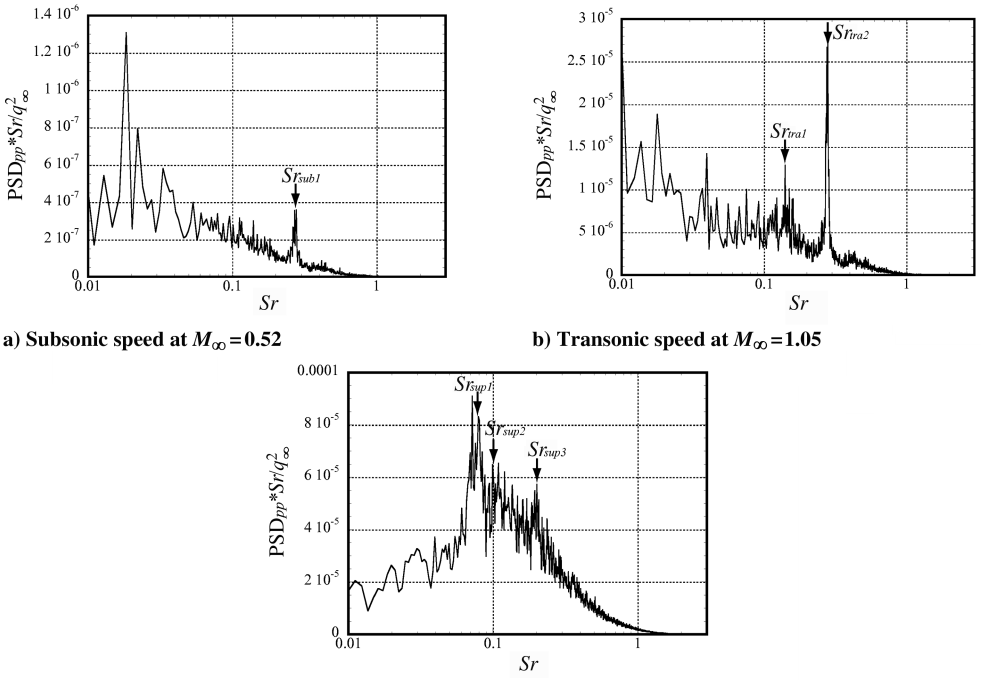

a) Subsonic speed at $M_\infty = 0.52$

b) Transonic speed at $M_\infty = 1.05$

c) Supersonic speed at $M_\infty = 3.00$

Fig. 7 One-sided PSDs vs Strouhal number of base pressure fluctuations at $r = 3/4R$.

are in fact contributed to by the location of the high-pressure region. When the freestream approaches sonic, the high-pressure region rapidly shifts toward the base while the pressure maintains approximately the same. Therefore, the high-pressure region induces a smaller recirculating region with stronger flow. As a result, the base pressure falls and the rms base pressure fluctuation increases.

C. Time-Series Characteristics of Base Pressure

Figure 7 shows one-sided PSDs of the base pressure fluctuations at $3/4R$ in the radial direction on the base surface as a function of Strouhal number for the cases of $M_\infty = 0.52$, 1.05, and 3.0, where PSD $\times$ Sr is normalized by the second power of the freestream dynamic pressure. Figure 7 is plotted on a semilog scale in the same manner as Janssen and Dutton [12]. Although not shown here, the PSDs at the subsonic speeds of $M_\infty = 0.52$ and 0.66, the transonic speeds of $M_\infty = 1.05$ and 1.2, and the supersonic speeds of $M_\infty =$ 2.0 and 3.0 are similar. These analyses help understand clearly the strong relationship between base flows and base pressure.

For subsonic speeds, one clear peak in the PSD occurs at the Strouhal number of Sr_{sub1} (0.28 for $M_\infty = 0.52$) as shown in Fig. 7a. In Fig. 7b, when the freestream reaches sonic condition, two clear peaks of base pressure fluctuation energy appear at Sr_{tra1} and Sr_{tra2} (0.14 and 0.28 for $M_\infty = 1.05$). As the flow furthermore increases into the supersonic regime, the main energy of the base pressure fluctuations shift to higher frequency compared with the spectra at the subsonic and transonic regimes. Three major peaks of base pressure fluctuation energy are visible at $Sr_{\text{sup 1}}$, $Sr_{\text{sup 2}}$, and $Sr_{\text{sup 3}}$ (0.075, 0.10, and 0.20 for $M_\infty = 3.0$) as shown in Fig. 7c. Similar PSD features also are obtained from the past experimental data of Janssen and Dutton [12] ($M_\infty = 2.46$ and $Re = 52 \times 10^6$ m^{-1}). To identify the dominant frequencies of the flowfields and the relationship between the flow mechanisms and characteristics of the base pressure, time-series, and time-averaged analyses in the flows downstream of the base are carried out in the following sections.

D. Characteristics of Base Flows at Subsonic Speeds

Instability of free shear layers in the axisymmetric base flows induces strong unsteadiness in the base flowfields in all subsonic cases. One-sided PSDs of the fluctuations of flow properties at $M_\infty = 0.52$ at selected locations are plotted in Fig. 8. Figure 8b shows the PSD of radial velocity fluctuations at point A. Strouhal number of the vortex shedding, induced by the instability of free shear layers, is about 0.28, which corresponds to the Strouhal number of the clear peak of base pressure fluctuation Sr_{sub1} as shown in Fig. 7a. In Fig. 8c, the PSD of static pressure fluctuations near the center of high-pressure region at point B displays a peak at $Sr_{\text{sub1}} = 0.28$. The result indicates that the pressure at the high-pressure region also fluctuates around $Sr_{\text{sub1}} = 0.28$ due to vortex shedding from the shear layer. PSDs of streamwise velocity fluctuations at point C (near the high-pressure region) and D (near the base) in Figs. 8d and 8e show that clear peaks of the energy fluctuation appear at the same Strouhal number for pressure fluctuations at the high-pressure region and large vortex shedding. The close relation in the spectra among the fluctuation of the high-pressure region, vortex shedding, and recirculating flow indicates that the pressure fluctuation at the high-pressure region pushes back the flow and induces the streamwise flow (reverse flow) inside the recirculating region. Furthermore, the results suggest that the large vortex structures in the wake and the associated flapping of the wake, which induces the fluctuation in the high-pressure region, also cause the backflow. As a result, one clear peak of the base pressure fluctuation energy at $Sr_{\text{sub1}} = 0.28$ is induced by the fluctuations of the circulating flows inside the recirculating region. According to the results, it is reasonable to suppose that the instability of shear layers, which causes the unsteady vortex shedding in the wake and the associated flapping of the wake, has dominant influences on the overall base flowfields at this subsonic speed. The present time-series analysis also supports our previous simplified finding that high-pressure region behind the base can be strongly related to the characteristics of base pressure.

Instantaneous vorticity magnitude and time-averaged Mach number distributions downstream of the base at $M_\infty = 0.52$ and 0.94 are shown in Fig. 9. Focusing on the unsteady vortex shedding induced by the instability of shear layers, which were found to have dominant influences on the subsonic base flowfields, there is a difference in the position where the instability of shear layers visually begins. At subsonic speeds, the position of the instability gradually moves downstream with increasing freestream Mach number. This phenomenon originates from the stabilizing effect of compressibility in the free shear layers with increasing (convective) Mach number as reported in the experimental and theoretical investigations of Papamoschou and Roshko [49] and Bogdanoff [50], and the

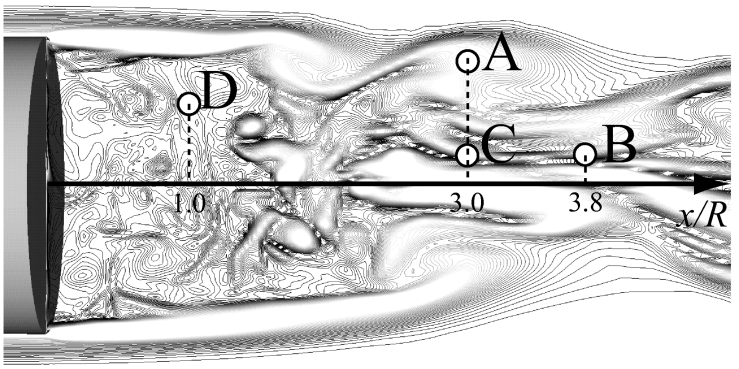

a) Locations of selected measurement points: vorticity magnitude distributions

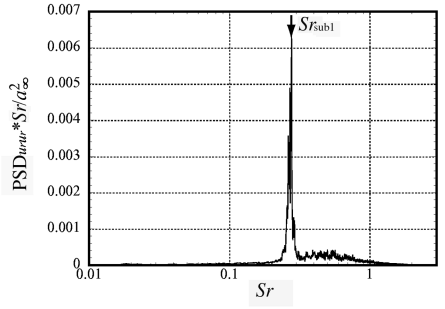

b) Point A: radial velocity fluctuations

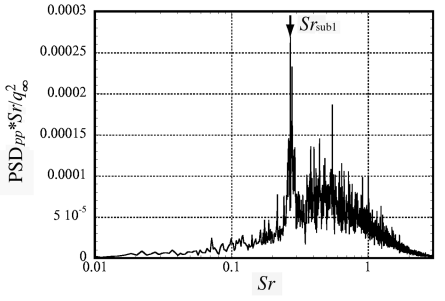

c) Point B: static pressure fluctuations

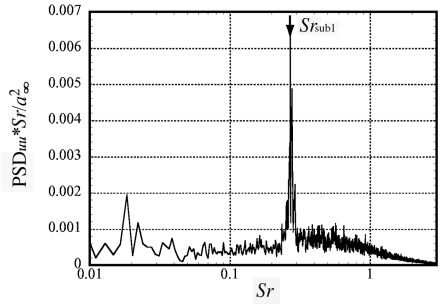

d) Point C: streamwise velocity fluctuations

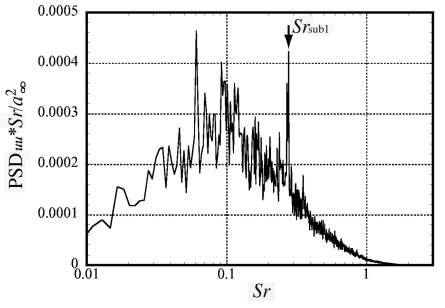

e) Point D: streamwise velocity fluctuations

Fig. 8 One-sided PSDs of the fluctuations of flow properties at the subsonic speed of $M_\infty = 0.52$.

numerical investigations of Sarkar [51] and Mitchell et al. [52]. The positional difference of the instability changes the location where the free shear layers begin to interfere with each other near the wake axis. Therefore, the location of initial interferences of the time-averaged free shear layers also gradually moves downstream with increasing freestream Mach number as illustrated in Fig. 9b. In Fig. 6, from the time-averaged point of view, the location of the high-pressure region also shifts downstream with increasing subsonic Mach numbers because the high-pressure region is generated by the interferences of shear layers. Although the location moves downstream with increasing freestream Mach number, the base pressure decreases proportionally with respect to the increasing dynamic pressure at the subsonic speeds because the strengthened high-pressure region induces strong circulating flow.

Time-averaged streamline patterns downstream of the base at $M_\infty = 0.94$ are shown in Fig. 10. The streamline patterns show two toroidal vortex patterns inside the recirculating region, a secondary separated region near the base, and two stagnation points on the wake

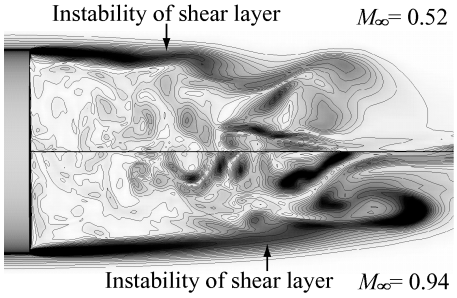

a) Instantaneous vorticity magnitude distributions

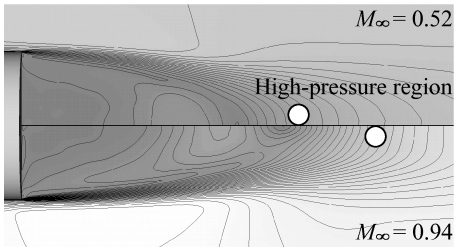

b) Time-averaged Mach number distributions

Fig. 9 Instantaneous and time-averaged base flowfields at $M_\infty = 0.52$ and 0.94.

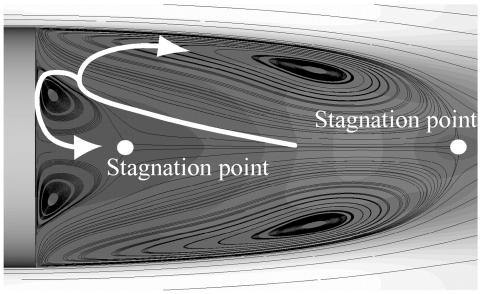

Fig. 10 Time-averaged streamline patterns downstream of the base edge at $M_\infty = 0.94$.

axis. This flow feature has also been observed and measured during the experimental investigation of subsonic base flows by Merz et al. [5].

E. Characteristics of Base Flows at Transonic Speeds

As the freestream Mach number increases pass the sonic threshold, front and rear local shock waves appear and oscillate in the streamwise direction along the free shear layers, which oscillate radially as illustrated in Fig. 11. These local shock waves seem to amplify the unsteadiness in the flow. One-sided PSDs of the fluctuations of flow properties as a function of Strouhal number at the transonic speed of $M_\infty = 1.05$ are plotted in Fig. 12. As clearly shown in PSDs of radial velocity fluctuations at point A (Fig. 12b) and static pressure fluctuations at point B (Fig. 12c), the free shear layer and front local shock wave oscillate at the same Strouhal number of 0.28, which corresponds to the Sr_{tra2} of the second peak of the base pressure fluctuation energy seen in Fig. 7b. The close relation in the spectra between the oscillation of the free shear layer and the front local shock wave indicates that small oscillations from the instability of free shear layers generate the front local shock wave, and then the adverse pressure gradient produced by this shock wave amplifies the instability of the free shear layers and induces vortex shedding. Similar to the subsonic case, the peak of PSD of static pressure fluctuations near the center of high-pressure region (point C) also appears at the Strouhal number of Sr_{tra2} as shown in Fig. 12d.

In Figs. 12e and 12f, as the measurement point moves from point D ($x/R = 3.2$) to point E ($x/R = 3.4$, time-averaged position of the rear shock wave), a peak of pressure fluctuation energy at the Strouhal number of Sr_{tra1} gradually appears whereas the peak at the Strouhal number of Sr_{tra2} remains intact. Because the first spectrum peak of Sr_{tra1} does not appear to be dominant and the frequency of Sr_{tra1} is half the frequency of Sr_{tra2}, it is reasonable to conclude that the first spectrum peak of Sr_{tra1} is a subharmonic peak of the main frequency at the second peak of Sr_{tra2}. The subharmonic peak of the pressure fluctuation energy corresponds to the first peak of base pressure fluctuation as illustrated in Fig. 7b. Because the spectra near the rear shock show two peaks, the PSD of the static pressure fluctuations at the root of the rear shock wave at the edge of the high-pressure region (point F) displays two major peaks at the Strouhal numbers of Sr_{tra1} and Sr_{tra2}, shown in Fig. 12g. Therefore, psd of streamwise velocity fluctuations at point G near the base, as shown in Fig. 12h, also shows two major peaks of the fluctuation energy content at the Strouhal numbers of Sr_{tra1} and Sr_{tra2}. As a result, the reverse flow fluctuations cause the two peaks of base pressure fluctuations where the spectrum peak of Sr_{tra1} is a subharmonic of the second peak of Sr_{tra2}.

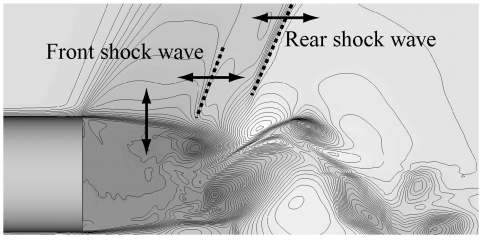

Fig. 11 Unsteadiness of a base flowfield at the transonic speed $M_\infty = 1.05$: density distributions.

Similar to the subsonic case, the correspondence of the Strouhal numbers between the fluctuations near the high-pressure region, vortex shedding, and the recirculating flow near the base indicates that the pressure fluctuation at the high-pressure region and the large vortex structures in the wake induce the reverse flow inside the recirculating region. According to this result, it is reasonable to suggest that the cause of the dominant unsteadiness in the flow is basically the same as the one in the subsonic case; that is, instability of the free shear layers induce the flow unsteadiness. A difference between the subsonic and transonic base flow is the appearance of local shock waves. The local shock waves rapidly amplify the instability and unsteadiness in the free shear layer, as well as induce the vortex shedding and the associated flapping of the wake. The sharply increased rms base pressure fluctuations at the transonic speed is due to the oscillating local shock waves.

Figure 13 shows the instantaneous density distributions downstream of the base at $M_\infty = 0.94$ and 1.05. Oscillating front and rear local shock waves suddenly appear on the free shear layers when the freestream Mach number slightly increases across sonic speed. Instantaneous vorticity magnitude at the same instance is shown in Fig. 14a. As the freestream Mach number approaches transonic and passes sonic speed, the position where the instability of free shear layers is generated moves rapidly toward the base because the sudden appearance of the front local shock wave produces adverse pressure gradient and amplifies the instability in the free shear layer. From the time-averaged point of view, the location of initial interferences of shear layers and the associated high-pressure region rapidly shifts upstream when the Mach number slightly increases at the transonic speeds as shown in Fig. 14b. As a consequence, the high-pressure region induces a small recirculating region with strong flow and the static pressure inside the recirculating region suddenly decreases. Therefore, the rapid decrease in base pressure near sonic speed as shown in Fig. 5 is realized.

Time-averaged streamline patterns downstream of the base at $M_\infty = 1.20$ are shown in Fig. 15. The streamline patterns still show two toroidal vortex patterns with two stagnation points similar to the time-averaged subsonic base flows, but the size of the secondary separated region in this case is smaller than the one in the subsonic case.

F. Characteristics of Base Flows at Supersonic Speeds

As the freestream Mach number increases from transonic to supersonic, the unsteady front local shock wave observed at transonic speeds disappears and a recompression process occurs along with the presence of an oblique shock wave. Similar to the subsonic and transonic base flows, the flowfield at supersonic speeds also shows strong unsteadiness due to the instabilities in the free shear layers and unsteady oscillations of the oblique shock wave. One-sided PSDs of the fluctuations of flow properties as a function of Strouhal number at $M_\infty = 3.00$ at selected locations are plotted in Fig. 16. As clearly shown in the PSD of radial velocity fluctuations at point A (Fig. 16b), two major peaks are visible at the Strouhal numbers of 0.10 and 0.20, which are identical to the Strouhal numbers of second and third peaks ($Sr_{\text{sup}\,2}$ and $Sr_{\text{sup}\,3}$) of the base pressure fluctuations seen in Fig. 7c. Plotted in Fig. 16c, a very similar PSD is obtained in the static pressure fluctuations at point B. The PSDs indicate that the fluctuations of the free shear layer induce the pressure fluctuations in the region between the expansion wave from the base edge and the recompression shock wave. Because the spectrum peak of $Sr_{\text{sup}\,2}$ does not appear to be dominant, the results imply that main frequency of the fluctuation of the free shear layer is the Strouhal number of $Sr_{\text{sup}\,3}$, and the peak of $Sr_{\text{sup}\,2}$ is subharmonic. When the measurement point is moved from point B to point C (location of oblique shock wave), the subharmonic peak of $Sr_{\text{sup}\,2}$ is not clearly visible in the spectra and only the main frequency of the pressure fluctuation energy content of $Sr_{\text{sup}\,3}$ is present as illustrated

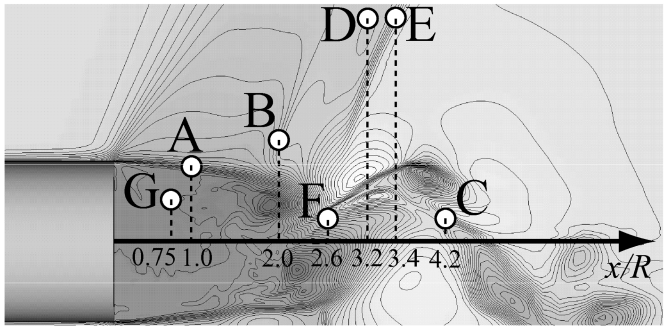

a) Locations of selected measurement points: density distributions

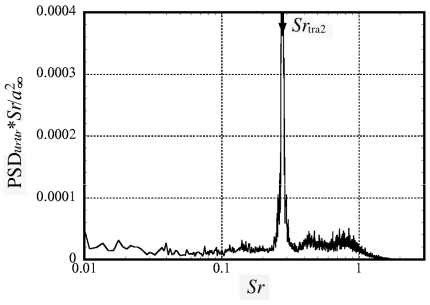

b) Point A: radial velocity fluctuations

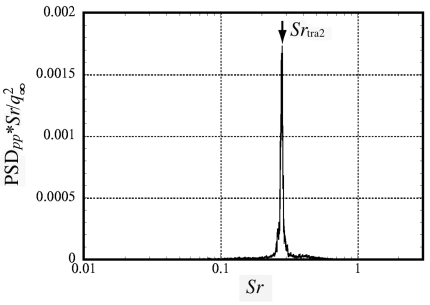

c) Point B: static pressure fluctuations

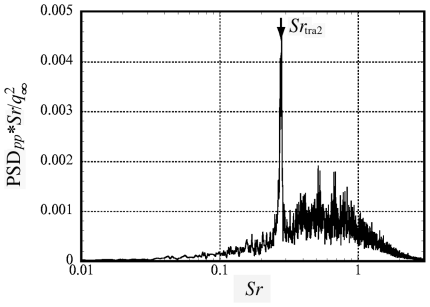

d) Point C: static pressure fluctuations

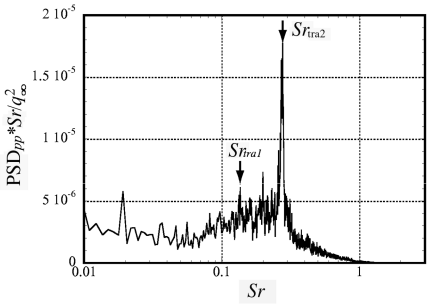

e) Point D: static pressure fluctuations

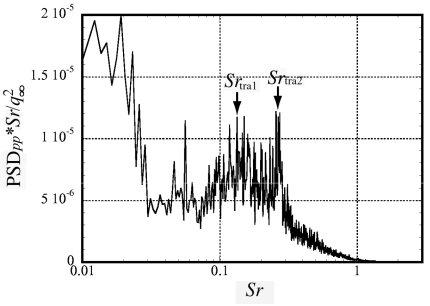

f) Point E: static pressure fluctuations

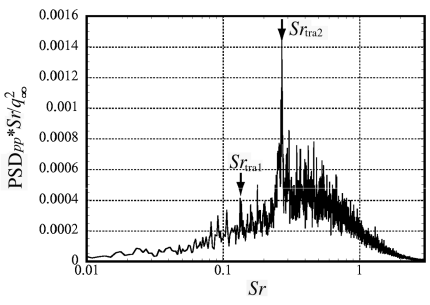

g) Point F: static pressure fluctuations

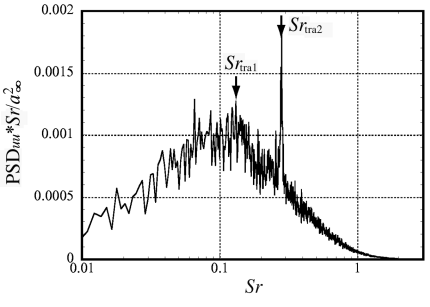

h) Point G: streamwise velocity fluctuations

Fig. 12 One-sided PSDs of the fluctuations of flow properties at the transonic speed $M_\infty = 1.05$.

in Fig. 16d. Similar to the transonic case, these results indicate that the oscillations originated from the instability of free shear layers induce the oscillations of the oblique shock wave.

Looking into the high-pressure region at point D and the root of the oblique shock wave at point E, three major peaks of the pressure fluctuation energy content are visible at the Strouhal number of $Sr_{\sup 1} = 0.075$, $Sr_{\sup 2} = 0.10$, and $Sr_{\sup 3} = 0.20$ as shown in Figs. 16e and 16f. The spectrum peak of $Sr_{\sup 3}$ and its subharmonic of $Sr_{\sup 2}$ originate from the instability of the free shear layer. The additional peak at $Sr_{\sup 1} = 0.075$ is not a subharmonic of the other peaks but an independent peak. These results suggest that an additional mechanism besides the instability of the free shear layer is possibly at work in the supersonic base flow. In Fig. 16g, PSD of the axial velocity fluctuation energy content at point F also demonstrates three major peaks at the Strouhal numbers of $Sr_{\sup 2}$, $Sr_{\sup 2}$, and $Sr_{\sup 3}$, which correspond to the peaks observed at the high-pressure region. The three major peaks of base pressure fluctuation energy, shown in Fig. 7c, are realized by the reverse flow fluctuations where the spectrum peaks of $Sr_{\sup 1}$ and $Sr_{\sup 3}$ are independent and the peak of $Sr_{\sup 2}$ is a subharmonic of the third peak. Similar to the subsonic and transonic base flows, instability of free shear layers has a dominant effect on the overall base flowfields. The time-series results also demonstrate that the pressure fluctuation at the high-pressure region and the large vortex structures in the wake induce the reverse

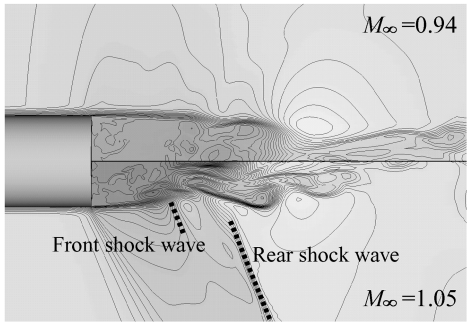

Fig. 13 Instantaneous density distributions at $M_\infty = 0.94$ and 1.05.

flow inside the recirculating region. Differing from the subsonic and transonic speeds, there seems to be an additional mechanism at work at this supersonic speed. At locations A, B, and C, only the shear layer frequency of Sr_{tra3} and its subharmonic at Sr_{tra2} are visible. On the other hand, at locations D, E, and F, there exists an additional spectrum peak with $Sr_{\text{sup 1}} = 0.075$, which is not a subharmonic of the other peaks. Because these three locations are all close to the wake axis, the possible mechanism of this independent frequency is due to instability within the recirculating region.

Time-averaged static pressure distributions and streamline patterns downstream of the base at $M_\infty = 1.50$ and 4.0 are shown in Fig. 17. It is well known that at supersonic speeds, the flow through an expansion wave at the base edge converges to the wake axis and the angle of the recompression shock wave to the freestream decreases with increasing freestream Mach number. One may expect the high-pressure region, produced by the free shear layer interferences around the wake axis, to shift toward the base with increasing Mach number because the free shear layers converge to the wake axis as the Mach number increases. However, the result shows that the high-pressure region moves downstream with increasing Mach number as shown in Fig. 6. Focusing on the free shear layer which has significant influences on the flowfield, the streamlines inside the free shear layers (white lines in Fig. 17) are seen gradually curved by the compression wave at the root of the oblique shock wave and tend to curve further downstream with increasing Mach number. As a result, the position of the high-pressure region slowly moves downstream with increasing freestream Mach number at the supersonic speeds. Although the location moves downstream with increasing Mach number, the base pressure gradually reduces toward an asymptotic value at increasing supersonic flow because the strengthened high-pressure region induces strong circulating flow.

Time-averaged streamline patterns downstream of the base at supersonic speeds show that the secondary separated region near the base, which appeared at the subsonic and transonic speeds, seems to gradually disappear when the freestream Mach number reaches beyond 1.5 in the present study. For this flow condition, only one toroidal vortex pattern inside the recirculating region is observed as shown in Fig. 17. For all computed cases, the maximum reverse flow velocities inside the recirculating flow are about 25% of the freestream velocity.

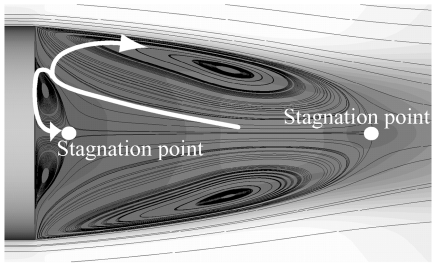

Fig. 15 Time-averaged streamline patterns downstream of the base at $M_\infty = 1.20$.

VI. Conclusions

Time-series and time-averaged characteristics of cylindrical base flows from subsonic to supersonic speeds at zero angle of attack were computationally investigated. Computations were performed by using a LES/RANS hybrid methodology. Time-series and time-averaged analyses are examined to give insight into the physics of base flows that dominantly influence the Mach number dependence of the base flows.

As the freestream Mach number increases, the base flows display three distinctive characteristics at subsonic, transonic and supersonic regimes. The normalized time-averaged base pressure decreases proportionally with respect to increasing freestream dynamic pressure in the subsonic regime when Mach numbers are less than 0.8. The base pressure begins to fall rapidly in the transonic regime. It then settles down and decreases gradually toward an asymptotic value at Mach numbers beyond 1.5. The normalized rms base pressure fluctuations sharply increase as the freestream Mach number approaches sonic speed, whereas they gradually decrease with increasing Mach number at subsonic regime below $M_\infty = 0.8$ and supersonic regime beyond $M_\infty = 1.5$.

The base pressure fluctuation energy contents show one clear peak at subsonic speeds (related to the shear layer dynamics), two clear peaks at transonic speeds (related to the shear layer dynamics and its subharmonic), and three major peaks at supersonic speeds (related to the shear layer dynamics, its subharmonic, and an additional mechanism).

Instability of free shear layers which causes the unsteady vortex shedding in the wake and the associated flapping of the wake has a dominant influence on the overall base flowfields over a wide range of Mach numbers ranging from subsonic to supersonic speeds. The structure of transonic base flows is different from the subsonic because of the presence of oscillating local shock waves. The unsteady local shock waves amplify the instability and unsteadiness in the free shear layer and cause the sharply increased rms base pressure fluctuations at the transonic speeds. Differing from the subsonic and transonic cases, there seem to be two separate mechanisms that affect the overall base flowfield at supersonic regime; the additional mechanism beside the free shear layer dynamics is probably the instability within the recirculating region because the corresponding spectrum peak is observed only close to the wake axis.

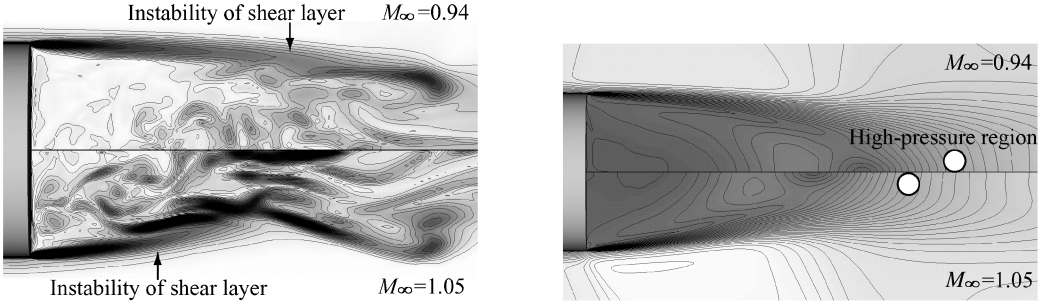

a) Instantaneous vorticity magnitude distributions **b) Time-averaged Mach number distributions**

Fig. 14 Instantaneous and time-averaged base flowfield at $M_\infty = 0.94$ and 1.05.

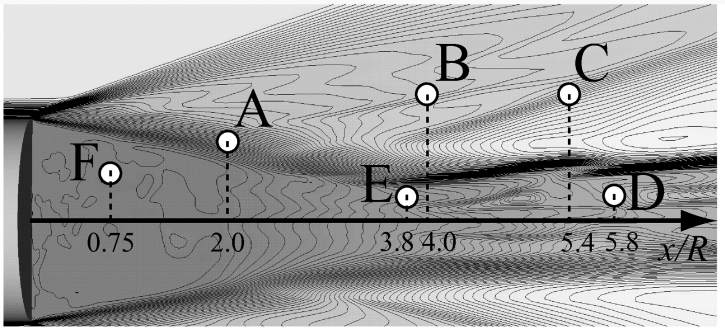

a) Locations of selected measurement points: density distributions

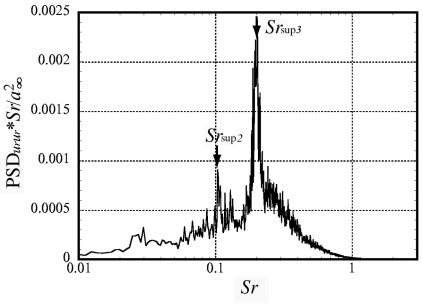

b) Point A: radial velocity fluctuations

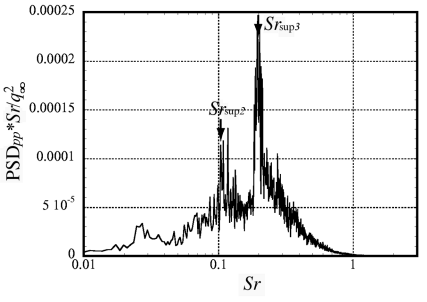

c) Point B: static pressure fluctuations

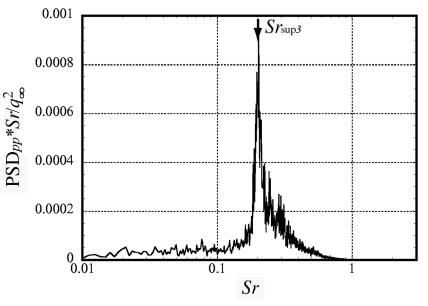

d) Point C: static pressure fluctuations

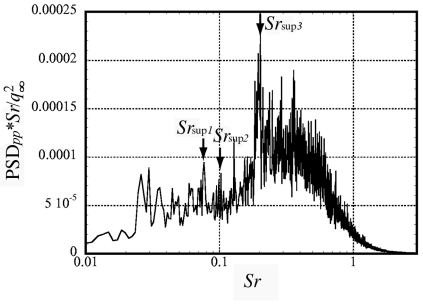

e) Point D: static pressure fluctuations

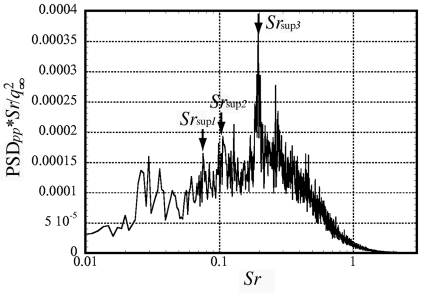

f) Point E: static pressure fluctuations

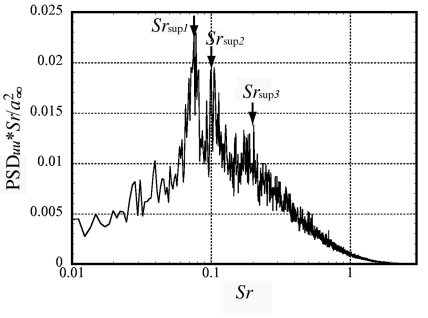

g) Point F: streamwise velocity fluctuations

Fig. 16 One-sided PSDs of fluctuations of flow properties at the supersonic speed of $M_\infty = 3.00$.

The high-pressure region downstream from the base is associated with the shear layer dynamics which has a dominant influence on the flowfields. The similar nature in the spectra of the pressure fluctuations at the high-pressure region, the shear layer dynamics, and recirculating flow suggests that the high-pressure region and the large vortex structures in the wake induce the circulating flow inside the recirculating region. Correspondence in the spectra of the circulating flow with the base pressure suggests that substantial base pressure fluctuation energy is contributed to by the fluctuation (pulsing) of the flow inside the recirculating region.

From the time-averaged point of view, the strong Mach number dependence of the base pressure is strongly related to the Mach number dependence of the location and magnitude of the highest pressure in the developing wake. The sharp decrease in base pressure at transonic speeds are attributed primarily by the location of the high-pressure region which shifts toward the base with even a slight increase in the freestream Mach number due to the sudden appearance of the oscillating local shock waves. The gradually decreasing base pressure at subsonic and supersonic speeds with respect to increasing freestream Mach number are the results of strengthened high-pressure regions that induce stronger circulating flows, whereas the location gradually moves downstream with increasing Mach number.

Streamline patterns in the time-averaged flowfields show two toroidal vortex patterns inside the recirculating region at Mach numbers below 1.5. The secondary separated region gradually becomes smaller and disappears when the freestream Mach number increases from subsonic to supersonic speeds, and one toroidal vortex pattern remains. The results show the possibility that the secondary separated region disappears with increasing Mach number.

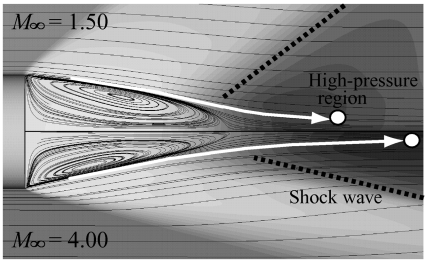

Fig. 17 Time-averaged static pressure distributions and streamline patterns at $M_\infty = 1.50$ and 4.0.

Acknowledgment

This work is partially supported by the Japan Society for the Promotion of Science (Project 16-10764). The first author would like to appreciate their support.

References

[1] Rollstin, L., "Measurement of In-Flight Base Pressure on an Artillery-Fired Projectile," *Journal of Spacecraft and Rockets*, Vol. 27, No. 1,

1990, pp. 5–6.
[2] Sahu, J., and Nietubicz, J. C., "Navier–Stokes Computations of Projectile Base Flow with and Without Mass Injection," *AIAA Journal*, Vol. 23, No. 9, 1985, pp. 1348–1355.
[3] Teramoto, S., and Fujii, K., "Mechanism of Dynamic Instability of a Reentry Capsule at Transonic Speeds," *AIAA Journal*, Vol. 40, No. 12, Dec. 2002, pp. 2467–2475.
[4] Lamb, J. P., and Oberkampf, L. W., "Review and Development of Base Pressure and Base Heating Correlations in Supersonic Flow," *Journal of Spacecraft and Rockets*, Vol. 32, No. 1, July 1995, pp. 8–23.
[5] Merz, R. A., Page, R. H., and Przirembel, C. E. G., "Subsonic Axisymmetric Near-Wake Studies," *AIAA Journal*, Vol. 16, No. 7, July 1978, pp. 656–662.
[6] Chow, W. L., "Base Pressure of a Projectile Within the Transonic Flight Regime," *AIAA Journal*, Vol. 23, No. 3, March 1985, pp. 388–395.
[7] Bulmer, B. M., "Flight-Test Base Pressure Measurements in Turbulent Flow," *AIAA Journal*, Vol. 14, No. 12, Dec. 1976, pp. 1783–1785.
[8] Zarin, N. A., "Base Pressure Measurements on Sharp and Blunt 9 Degree Cones at Mach Numbers from 3.50 to 9.20," *AIAA Journal*, Vol. 4, No. 4, April 1966, pp. 743–745.
[9] Herrin, J. L., and Dutton, J. C., "Supersonic Base Flow Experiments in the Near-Wake of a Cylindrical Afterbody," *AIAA Journal*, Vol. 32, No. 1, Jan. 1994, pp. 77–83.
[10] Bourdon, C. J., and Dutton, J. C., "Planar Visualizations of Large-Scale Turbulent Structures in Axisymmetric Supersonic Separated Flows," *Physics of Fluids*, Vol. 11, No. 1, Jan. 1999, pp. 201–213.
[11] Boswell, A. B., and Dutton, J. C., "Velocity Measurements in a Three-Dimensional Compressible Base Flow," *AIAA Journal*, Vol. 41, No. 5, May 2003, pp. 785–794.
[12] Janssen, J. R., and Dutton, J. C., "Time-Series Analysis of Supersonic Base-Pressure Fluctuations," *AIAA Journal*, Vol. 42, No. 3, March 2004, pp. 605–613.
[13] Benay, R., and Servel, P., "Two-Equation k–σ Turbulence Model: Application to a Supersonic Base Flow," *AIAA Journal*, Vol. 39, No. 3, March 2001, pp. 407–416.
[14] Chuang, C. C., and Chieng, C. C., "Supersonic Base-Flow Computation Using Higher-Order Closure Turbulence Models," *Journal of Spacecraft and Rockets*, Vol. 33, No. 3, May–June 1996, pp. 374–380.
[15] Papp, J. L., and Ghia, K. N., "Application of the RNG Turbulence Model to the Simulation of Axisymmetric Supersonic Separated Base Flows," AIAA Paper 2001-0727, Jan. 2001.
[16] Tucker, P. K., and Shyy, W., "Numerical Analysis of Supersonic Flow over an Axisymmetric Afterbody," AIAA Paper 93-2347, June 1993.
[17] Schwane, R., Hagemann, G., and Reijasse, P., "Plug Nozzles: Assessment of Prediction Methods for Flow Features and Engine Performance," AIAA Paper 2002-0585, Jan. 2002.
[18] Paciorri, R., Nasuti, F., and Sabetta, F., "Evaluation of Turbulence Modeling in Supersonic Afterbody Computations," AIAA Paper 2001-3039, June 2001.
[19] Bakker, P. G., and Bannink, W. J., "CFD Validation for Base Flows with and Without Plume Interaction," AIAA Paper 2002-0438, Jan. 2002.
[20] Fureby, C., Nilsson, Y., and Andersson, K., "Large Eddy Simulation of Supersonic Base Flow," AIAA Paper 99-0426, Jan. 1999.
[21] Baurle, A. R., and Tam, J. C., "Hybrid Simulation Approach for Cavity Flows: Blending, Algorithm, and Boundary Treatment Issues," *AIAA Journal*, Vol. 41, No. 8, Aug. 2003, pp. 1463–1480.
[22] Spalart, P. R., "Strategies for Turbulence Modeling and Simulations," *International Journal of Heat and Fluid Flow*, Vol. 21, No. 3, 2000, pp. 252–263.
[23] Spalart, P. R., and Allmaras, S. R., "One-Equation Turbulence Model for Aerodynamic Flows," AIAA Paper 92-0439, Jan. 1992.
[24] Kawai, S., and Fujii, K., "Computational Study of Supersonic Base Flow Using Hybrid Turbulent Methodology," *AIAA Journal*, Vol. 43, No. 6, June 2005, pp. 1265–1275.
[25] Kawai, S., and Fujii, K., "Analysis and Prediction of Thin-Airfoil Stall Phenomena Using Hybrid Turbulent Methodology," *AIAA Journal*, Vol. 43, No. 5, May 2005, pp. 953–961.
[26] Vreman, A. W., "Direct and Large-Eddy Simulation of the Compressible Turbulent Mixing Layer," Ph.D. Thesis, University of Twente, The Netherlands, Dec. 1995.
[27] Cebeci, T., and Smith, A. M. O., *Analysis of Turbulent Boundary Layers*, Academic Press, New York, 1974.
[28] Lund, S. T., Wu, X., and Squires, D. K., "Generation of Turbulent Inflow Data for Spatially-Developing Boundary Layer Simulations," *Journal of Computational Physics*, Vol. 140, No. 2, March 1998, pp. 233–258.
[29] Spalart, P. R., "Young-Person's Guide to Detached-Eddy Simulation Grids," NASA CR-2001-211032, July 2001.
[30] Smagorinsky, J., "General Circulation Experiments with the Primitive Equations, Part 1: The Basic Experiment," *Monthly Weather Review*, Vol. 91, No. 3, March 1963, pp. 99–152.
[31] Scotti, A., and Meneveau, C., "Generalized Smagorinsky Model for Anisotropic Grids," *Physics of Fluids A*, Vol. 5, No. 9, 1993, pp. 2306–2308.
[32] Yoshizawa, A., "Statistical Theory for Compressible Turbulent Shear Flows, with the Application to Subgrid Modeling," *Physics of Fluids*, Vol. 29, No. 7, July 1986, pp. 2152–2164.
[33] Moin, P., Squires, K., Cabot, W., and Lee, S., "Dynamic Subgrid-Scale Model for Compressible Turbulence and Scalar Transport," *Physics of Fluids A*, Vol. 3, No. 11, Nov. 1991, pp. 2746–2757.
[34] Vreman, B., Geurts, B., and Kuerten, H., "A Priori Tests of Large Eddy Simulation of the Compressible Plane Mixing Layer," *Journal of Engineering Mathematics*, Vol. 29, No. 4, July 1995, pp. 299–327.
[35] Vreman, B., Geurts, B., and Kuerten, H., *Subgrid-Modeling in LES of Compressible Flow, Direct and Large-Eddy Simulation 1*, Kluwer Academic, Norwell, MA, 1994.
[36] Vreman, B., Geurts, B., and Kuerten, H., "Realizability Conditions for the Turbulent Stress Tensor in Large-Eddy Simulation," *Journal of Fluid Mechanics*, Vol. 278, Nov. 1994, pp. 351–362.
[37] Rogallo, R. S. and Moin, P., "Numerical Simulation of Turbulent Flows," *Annual Review of Fluid Mechanics*, Vol. 16, Jan. 1984, pp. 99–137.
[38] Baldwin, B., and Lomax, H., "Thin Layer Approximation and Algebraic Model for Separated Turbulent Flows," AIAA Paper 78-257, Jan. 1978.
[39] Shima, E., and Jounouchi, T., "Role of CFD in Aeronautical Engineering (No. 14) AUSM Type Upwind Schemes," *Proceedings of the 14th NAL Symposium on Aircraft Computational Aerodynamics*, National Aeronautical Lab., Bangalore, India, 1997, pp. 7–12.
[40] van Leer, B., "Towards the Ultimate Conservative Difference Scheme 5: A Second-Order Sequel to Godunov's Method," *Journal of Computational Physics*, Vol. 32, No. 1, 1979, pp. 101–136.
[41] Choi, H., and Moin, P., "Effects of the Computational Time Step on Numerical Solutions of Turbulent Flow," *Journal of Computational Physics*, Vol. 113, No. 1, 1994, pp. 1–4.
[42] Yoon, S., and Jameson, A., "Lower-Upper Symmetric-Gauss-Seidel Method for the Euler and Navier–Stokes Equations," *AIAA Journal*, Vol. 26, No. 9, 1988, pp. 1025–1026.
[43] Chakravarthy, S. R., "Relaxation Methods for Unfactored Implicit Upwind Schemes," AIAA Paper 84-0165, Jan. 1984.
[44] Urbin, G., and Knight, D., "Large-Eddy Simulation of a Supersonic Boundary Layer Using an Unstructured Grid," *AIAA Journal*, Vol. 39, No. 7, 2001, pp. 1288–1295.
[45] Kawai, S., and Fujii, K., "Computational Analysis of the Characteristics of Subsonic, Transonic, and Supersonic Base Flows," AIAA Paper 2005-5156, June 2005.
[46] Shvets, A. I., "Base Pressure Fluctuations," *Fluid Dynamics*, Vol. 14, No. 3, 1979, pp. 394–401, 605–613.
[47] Kruiswyk, R. W., and Dutton, J. C., "Effects of a Base Cavity on Subsonic Near-Wake Flow," *AIAA Journal*, Vol. 28, No. 11, Nov. 1990, pp. 1885–1893.
[48] Molezzi, M., and Dutton, J. C., "Study of Subsonic Base Cavity Flowfield Structure Using Particle Image Velocimetry," *AIAA Journal*, Vol. 33, No. 2, Feb. 1995, pp. 201–209.
[49] Papamoschou, D., and Roshko, A., "Compressible Turbulent Shear Layer: An Experimental Study," *Journal of Fluid Mechanics*, Vol. 197, Dec. 1988, pp. 453–477.
[50] Bogdanoff, D. W., "Compressibility Effects in Turbulent Shear Layers," *AIAA Journal*, Vol. 21, No. 6, June 1983, pp. 926–927.
[51] Sarkar, S., "Stabilizing Effect of Compressibility in Turbulent Shear Flow," *Journal of Fluid Mechanics*, Vol. 282, Jan. 1995, pp. 163–186.
[52] Mitchell, B. E., Lele, S. K., and Moin, P., "Direct Computation of the Sound Generated by Vortex Pairing in an Axisymmetric Jet," *Journal of Fluid Mechanics*, Vol. 383, March 1999, pp. 113–142.

D. Gaitonde
Associate Editor